



Epitaxial growth and structure of LaVO 3 and PrVO 3 thin films

G. Masset, O. Copie, J. Ghanbaja, Karine Dumesnil, L. Pasquier, D. Pierre, S. Andrieu

► To cite this version:

G. Masset, O. Copie, J. Ghanbaja, Karine Dumesnil, L. Pasquier, et al.. Epitaxial growth and structure of LaVO 3 and PrVO 3 thin films. *Physical Review Materials*, 2020, 4 (6), 10.1103/PhysRevMaterials.4.064417 . hal-02887536


HAL Id: hal-02887536

<https://hal.science/hal-02887536>

Submitted on 20 Nov 2020

HAL is a multi-disciplinary open access archive for the deposit and dissemination of scientific research documents, whether they are published or not. The documents may come from teaching and research institutions in France or abroad, or from public or private research centers.

L'archive ouverte pluridisciplinaire **HAL**, est destinée au dépôt et à la diffusion de documents scientifiques de niveau recherche, publiés ou non, émanant des établissements d'enseignement et de recherche français ou étrangers, des laboratoires publics ou privés.

Epitaxial growth and structure of LaVO_3 and PrVO_3 thin filmsG. Masset , O. Copie *, J. Ghanbaja, K. Dumesnil, L. Pasquier, D. Pierre, and S. Andrieu
Institut Jean Lamour, CNRS/Université de Lorraine (UMR 7198), F-54000 Nancy, France(Received 13 January 2020; revised manuscript received 6 May 2020; accepted 29 May 2020;
published 22 June 2020)

We report on the epitaxial growth of PrVO_3 and LaVO_3 by molecular beam epitaxy on (001)-oriented SrTiO_3 substrates. We show that a high control of the deposition is achieved and leads to a highly reproducible layer-by-layer growth mode. We evidence also the effect of epitaxial strain on the magnetic properties of the epitaxial films. High-resolution transmission electron microscopy and scanning transmission electron microscopy observations reveal that an antipolar motion of the rare earth atoms exists in both LaVO_3 and PrVO_3 thin films. The investigation of the structural distortions and atomic displacements in the vanadate thin films may be generalized to other orthorhombic perovskite oxides and contributes to the search of ferroelectricity *by design* in symmetry-breaking magnetic oxide superlattices.

DOI: [10.1103/PhysRevMaterials.4.064417](https://doi.org/10.1103/PhysRevMaterials.4.064417)

I. INTRODUCTION

Structural distortions and the associated atomic displacements in transition metal oxides (TMO) with an oxide perovskite structure ABO_3 contribute to the interplay between the charge, orbital, and spin degrees of freedom of the electrons [1–3]. Beyond the ideal cubic and undistorted structure, the most common ABO_3 crystallographic symmetry is the orthorhombic $Pbnm$ one. It results from the ability of the ABO_3 family to adapt to a mismatch between AO and BO bond lengths, which is described by the geometric tolerance factor $t = (\text{AO}) = 2\sqrt{\text{BO}}$. Whereas the B – O – B bond angle remains 180° for $t = 1$ (cubic) and $t > 1$ (tetragonal), it decreases from 180° for $t < 1$ (orthorhombic or lower). Consequently, $t < 1$ yields cooperative oxygen octahedron rotations, or antiferrodistortive (AFD) motions, and relates typically to, e.g., RVO_3 series (R being a rare-earth or yttrium atom) among others. For example, cooperative VO_6 octahedron rotations lead to an orthorhombic $Pbnm$ structure with an $a^-a^-c^+$ tilt pattern according to Glazer's notation (out-of-phase rotation along the in-plane pseudocubic axes and in-plane rotation along the out-of-plane pseudocubic axis) for all members of the RVO_3 series at room temperature [4]. At low temperature, superexchange interactions stabilize then a C-type antiferromagnetic spin order (C-SO) of the V spins at a transition temperature T_{SO} . As R^{3+} ionic size decreases, cooperative octahedral site rotations increases. The V $3d - \text{O } 2p$ orbitals overlap integral is thus reduced and T_{SO} decreases monotonously with the R^{3+} ionic size as for other orthorhombic perovskites such as RCrO_3 or RFeO_3 [5]. Yet, oxygen octahedra are not rigid in $Pbnm$ perovskites and the atomic displacements are more than those induced by AFD motions. It is also epitomized in RVO_3 by an intrinsic site distortion that consists essentially in long and short V – O bonds length along the [100] and [010] pseudocubic directions [6]. The

Jahn-Teller (JT) distortion of the octahedra allows lifting the degeneracy between the JT active V t_{2g} levels. The two electrons per V^{3+} sites are either located in the d_{xy} and d_{xz} or in the d_{xy} and d_{yz} orbitals in an ideal picture. We note that, compared to $\text{Mn}^{3+} e_g$ electrons in RMnO_3 , the relative weak JT effect of the two t_{2g} electrons at V^{3+} sites has a subtle influence on physical properties such as biasing the orbital ordering [7]. Indeed, V t_{2g} occupied orbitals adopt a G-type order (G-OO) at the temperature $T_{\text{OO}} > T_{\text{SO}}$, concomitantly with a structural phase transition (orthorhombic $Pbnm$ to monoclinic $P2_1/m$) [4,8]. Such an intrinsic octahedral-site distortion is also responsible for spin-ordering transitions as, e.g., in RMnO_3 and RTiO_3 [9,10]. All these atomic displacements promoted by structural distortions modify the orbital occupancy and electron transfer between neighboring atoms and can give rise to complex orbital and spin order phase diagrams in TMO perovskites [8,10,11].

Here, we report on the epitaxial growth of PrVO_3 (PVO) and LaVO_3 (LVO) by molecular beam epitaxy on (001)-oriented SrTiO_3 substrates. We show that a high control of the deposition is achieved using molecular beam epitaxy (MBE) and leads to a highly reproducible layer-by-layer growth mode. We investigate the effect of the substrate-induced strains on the magnetic properties of the epitaxial films and, most of all, evidence $\text{Pr}(\text{La})$ displacements across the PVO(LVO) films using high-resolution transmission electron microscopy and scanning transmission electron microscopy. These atomic displacements correspond to an antipolar motion of the R^{3+} cations occurring in $Pbnm$ systems. These are important for tailoring hybrid improper ferroelectricity [12–14] *by design* as proposed in symmetry-breaking RVO_3 based superlattices [15].

Owing to the change of the AO covalency, the oxygen octahedra rotations impose a shift of R^{3+} respect to its position in cubic symmetry. Although AFD motions are non-polar and R^{3+} motions are antipolar in consecutive (001) planes, Varignon *et al.* proposed recently the occurrence of hybrid improper ferroelectricity in short-period ($\text{RVO}_3/\text{R}'\text{VO}_3$)

*olivier.copie@univ-lorraine.fr

superlattices and predicted an electrical control of orbital orderings in those systems [15]. The ferroelectric character may arise in the superlattice due to coupled VO_6 rotations ($a^-a^-c^+$ being $\phi_{xy}^- + \phi_z^+$ rotations) and $\text{R}(\text{R}')$ cation antipolar motions (X_5^- mode) via a trilinear term $\phi_{xy}^- X_5^- \phi_z^+$ in the free energy expansion. Since R and R' dipoles are uncompensated, X_5^- motion becomes a polar motion P_{xy} . The proposed mechanism provides a concrete way to design ferroelectricity in otherwise nonferroelectric $Pbnm$ orthorhombic oxides. Moreover, an electric control may be achieved in RVO_3 -based systems due to the intimate coupling of the spin and orbital orders with the lattice [8,9] and especially via JT motions [15]. The near degeneracy of orbital and spin orders makes indeed the RVO_3 properties highly tunable by external stimuli [8,16–18].

Renewed interests in RVO_3 have gained much attention owing to the possibilities of tailoring t_{2g} orbital physics with interesting magnetic [19], optical [20,21] and electronic properties [22,23]. So far, RVO_3 films have been grown by pulsed laser deposition (PLD) [24] or by MBE [25]. While the effect of strain on the VO_6 octahedra rotations [26,27] or La motions have also been investigated in LVO thin films grown by PLD [28], tunable magnetic properties has been observed in PVO thin films either as a function of the epitaxial strain [29,30] or the chemical strain through the control of oxygen vacancy concentration [31,32].

II. EXPERIMENTAL DETAILS

At room temperature, the refined bulk lattice parameters using high-resolution diffraction experiments [4] are $a_o = 5.487$ Å, $b_o = 5.564$ Å, $c_o = 7.779$ Å for PVO and $a_o = 5.555$ Å, $b_o = 5.553$ Å, $c_o = 7.847$ Å for LVO (o stands for orthorhombic). Then, considering a pseudocubic unit cell approximation, $a_p \approx a_o/\sqrt{2} \approx b_o/\sqrt{2} \approx c_o/2$, the averaged subcell parameter a_p is 3.901 and 3.926 Å for PVO and LVO, respectively. The thin films were grown onto (001)-oriented SrTiO_3 cubic substrates ($a_s = 3.905$ Å) using oxide-MBE. The lattice mismatch between a_p and a_s is thus +0.1% (tensile strain) and −0.5% (compressive strain) for PVO and LVO, respectively. We note also that the orbital and spin orderings take place at $T_{\text{OO}} \approx 180$ K and $T_{\text{SO}} \approx 135$ K for bulk PVO and at $T_{\text{OO}} \approx 140$ K and $T_{\text{SO}} \approx 140$ K for bulk LVO [8].

The STO substrates were rinsed using acetone and ethanol. Then, they were introduced in the MBE chamber (DCA Instruments) with a base pressure of 6×10^{-11} mbar, connected the Tube-Davm at the IJL. Atoms are evaporated using high temperature Knudsen cells and prior to the film deposition, the atomic fluxes are calibrated using a quartz crystal microbalance. The Pr, La, and V atomic fluxes were fixed to 1.5×10^{13} atom $\text{cm}^{-2} \text{s}^{-1}$ with 5% accuracy. The growth conditions have been optimized to obtain high quality single phase films. To get the proper oxygen stoichiometry, an oxidant gas ($\text{O}_3 + \text{O}_2$) was introduced at a pressure fixed in the $5\text{--}7 \times 10^{-7}$ mbar range in the chamber. During the growth, the substrate temperature was kept at 920 and 850 °C for PVO and LVO, respectively. The film growth was monitored using *in situ* reflection high-energy electron diffraction (RHEED).

The crystallinity and the structure were characterized by x-ray diffraction (XRD) with a PANalytical X'pert Pro

MRD diffractometer using monochromatic $\text{Cu } K\alpha_1$ radiation ($\lambda = 1.54056$ Å). Together with RHEED intensity oscillations, x-ray reflectivity (XRR) has been used to check the film thickness. The atomically resolved microstructure was determined by cross-sectional high-resolution transmission electron microscopy (HRTEM) and high angle annular dark field (HAADF) scanning transmission electron microscopy (STEM). The cross-section lamella were prepared by focus ion beam with Ga^+ ion milling (FEI-Helios Nanolab 600i) and observed with a double-aberration corrected JEOL ARM microscope operated at 200 kV. Magnetic measurements were performed using a Quantum Design superconducting quantum interference device magnetometer (MPMS3).

III. RESULTS AND DISCUSSION

The RHEED diffraction patterns along the [100], [110], and [210] azimuthal surface directions are displayed in Fig. 1, for STO (a), PVO (b), and LVO (c). The main streaks of the PVO and LVO patterns correspond to the STO ones, which prove the epitaxial growth of LVO and PVO onto (001)-STO substrate. In Fig. 1(d), we show the intensity of the diffraction spot recorded during the growth of PVO and LVO. The intensity oscillations are characteristic of a layer-by-layer growth mode for both materials. Moreover, from the very beginning of the deposition [see inset of Fig. 1(d)], these oscillations are clearly visible during the full deposition time (130 and 135 unit cells for PVO and LVO, respectively). Using atomic force microscopy measurements (see Supplemental Material [33]), we deduce a root-mean-square surface roughness of 3–4 Å for PVO and LVO.

Considering the cation's fluxes and assuming a stoichiometric oxygen content incorporated during the growth onto STO, we calculate the total flux for a pseudocubic cell (5 atoms) Φ_{tot} as 7.5×10^{13} atom $\text{cm}^{-2} \text{s}^{-1}$. The time τ for the completion of one pseudo-cubic unit cell (one RHEED intensity oscillation period) is given by $\Phi_{\text{tot}} = v_{\text{tot}} \times \rho_{\text{RVO}_3}$ with v_{tot} and ρ_{RVO_3} being the growth rate and the atomic density of the pseudocubic unit cell. $v_{\text{tot}} = a_{\perp}/\tau = \Phi_{\text{tot}}/\rho_{\text{RVO}_3}$ with a_{\perp} the out-of-plane pseudocubic lattice parameter. So, we find that the oscillation period $\tau = 5/(a_s^2 \times \Phi_{\text{tot}})$ is 43.7 ± 4.4 s (considering the fluxes accuracy). This has to be compared to 44.8 ± 0.4 s and 45.4 ± 0.9 s RHEED intensity oscillation periods observed during the LVO and PVO growth, respectively. This demonstrates the stoichiometric incorporation of oxygen atoms in the PVO and LVO films, within our experimental accuracy. According to the number of oscillations observed during the growth and a_{\perp} measured by XRD (see below), the total thickness is 506 Å for PVO and 533 Å for LVO. This is in excellent agreement with 505 and 523 ± 10 Å determined by XRR from the observed oscillation of the reflected intensity [see Fig. 1(e)]. All these results confirm the very good control of the stoichiometry in our films.

Also, the RHEED patterns of the PVO and LVO film surface exhibit extra diffraction streaks that are not related to a simple perovskite lattice. For both, half-order streaks are observed in the [100], [110], and [210] directions and are indicated by white arrows in Fig. 1(b). These superstructure streaks are characteristic of a double unit cell lying along the [100] (2×1) or the [010] (1×2) directions, corresponding

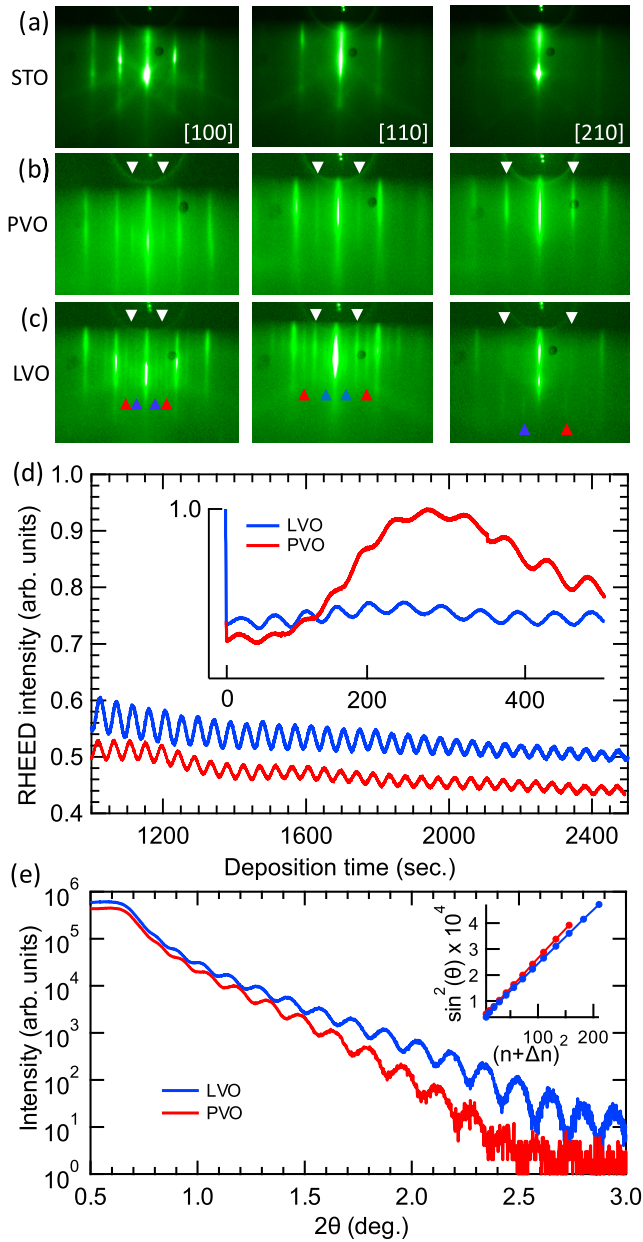


FIG. 1. RHEED observations along $[100]$, $[110]$, and $[210]$ azimuths on (a) the STO substrate surface, (b) the PVO as-grown surface, and (c) the LVO as-grown surface. The white arrows highlight the half streaks due to the orthorhombic PVO and LVO cells corresponding to a 2×2 pattern. The blue and red arrows indicate the reflections attributed to a 3×3 surface pattern. (d) RHEED intensity oscillations recorded during the deposition. One oscillation corresponds to one pseudo-cubic unit cell. The inset shows the oscillations at the beginning of the depositions. From the very start of depositions the 2D growth mode and the oscillations are obtained. (e) XRR measurements. Inset: maximum positions as a function of $(n + \Delta n)^2$ using $(\sin\theta)^2 \propto (n + \Delta n)^2 (\lambda/2t)^2$ to determine the film thickness (t).

to a 2×2 reconstruction. As $c_o \approx 2a_s$, it would agree with the PVO and LVO $[001]_o$ direction lying either along the STO $[100]$ or $[010]$ directions. For LVO, additional streaks (indicated by red and blue arrows, in Fig. 1(c) along $[100]$

and $[110]$) are also observed and would correspond to a 3×3 or 4×4 reconstruction. The reliability of monitoring *in situ* RHEED patterns for the characterization of the cation surface stoichiometry have been shown for LVO thin films grown by MBE [25]. Only stoichiometric LVO films exhibit indeed superstructure streaks, whereas La-rich and V-rich films display a spotty pattern and high background intensity, respectively. Zhang *et al.* have attributed the 2×2 reconstruction to a cubic symmetry lowering [25] (due to AFD motions and La and Pr displacements) as we have inferred by anticipating the $[001]_o$ direction parallel to the STO surface. Figure 2 displays the results of XRD measurements carried out on PVO and LVO thin films grown in optimized conditions. In Fig. 2(a), the symmetric θ - 2θ patterns indicate that the PVO and LVO films are single phase within the temperature and ozone partial pressure conditions used for the growth. In Fig. 2(b), high-resolution XRD measurements around the (002) Bragg's peak exhibit Laue fringes that confirm the good film crystallinity together with a well-defined film/substrate interface. The fit and analysis of the (002) Bragg's peak positions yields an out-of-plane lattice parameter a_\perp of 3.893 and 3.950 Å for PVO and LVO, respectively. From the rocking curve of $(002)_p$ reflections (not shown) we deduced a full width at half maximum $\Delta\omega \approx 0.075^\circ$ and $\Delta\omega \approx 0.023^\circ$ for the vanadate films and the substrate, respectively.

We show a representative reciprocal space map around the film and substrate asymmetrical $(103)_p$ Bragg's peaks in Figs. 2(c) and 2(d) for PVO and LVO, respectively. PVO and STO superimposed Bragg's peaks and LVO and STO Bragg's peaks aligned along the vertical dashed line indicate that both films are fully strained by the substrate. φ -scans measured for the LVO film and the substrate indicate that, in the pseudocubic description, the film adopts the fourfold symmetry of the STO plane [Fig. 2(e)]. Since the films are epitaxially constrained by the substrate, we can rationalize the substrate-induced film deformation. Based on in-plane epitaxial strain (ϵ_\parallel) and Poisson's ratio (ν) [29], we can calculate the expected out-of-plane lattice parameter $a_\perp = [1 - 2\nu\epsilon_\parallel / (1 - \nu)]a_p$, with $\epsilon_\parallel = (a_s - a_p)/a_p$. With $\nu = 0.3 - 0.398$ [29,34], it yields $a_\perp = 3.896$ Å and 3.955 Å for PVO and LVO, respectively. This is in very good agreement with the values extracted from θ - 2θ measurements and further indicates that the films are stoichiometric in oxygen. The oxygen vacancies would otherwise induce an additional tensile strain (up to 3%) along the growth direction [32].

The magnetic properties of PVO and LVO thin films have been then investigated. We note that the orbital and spin orderings in RVO_3 are very sensitive to changes in cation composition or disorder [16,35] and oxygen stoichiometry [32], which can destabilize the spin and orbital orders. In Fig. 3, we present the temperature dependence of the magnetization for PVO and LVO films. We observe a magnetic signal rising around 132 K for PVO and 150 K for LVO, which we attribute to the spin ordering at T_{SO} . We point out that despite an antiferromagnetic spin order expected at low temperature, antisymmetric spin-spin interactions via Dzyaloshinskii-Moriya interactions promote a canted and uncompensated spin state [19,36,37]. Together with the spin imbalance of the V $3d$ -V $3d$ sublattices [38], V $3d$ -R $4f$ magnetic exchange interactions [39–41] may also strengthen the ferromagneticlike

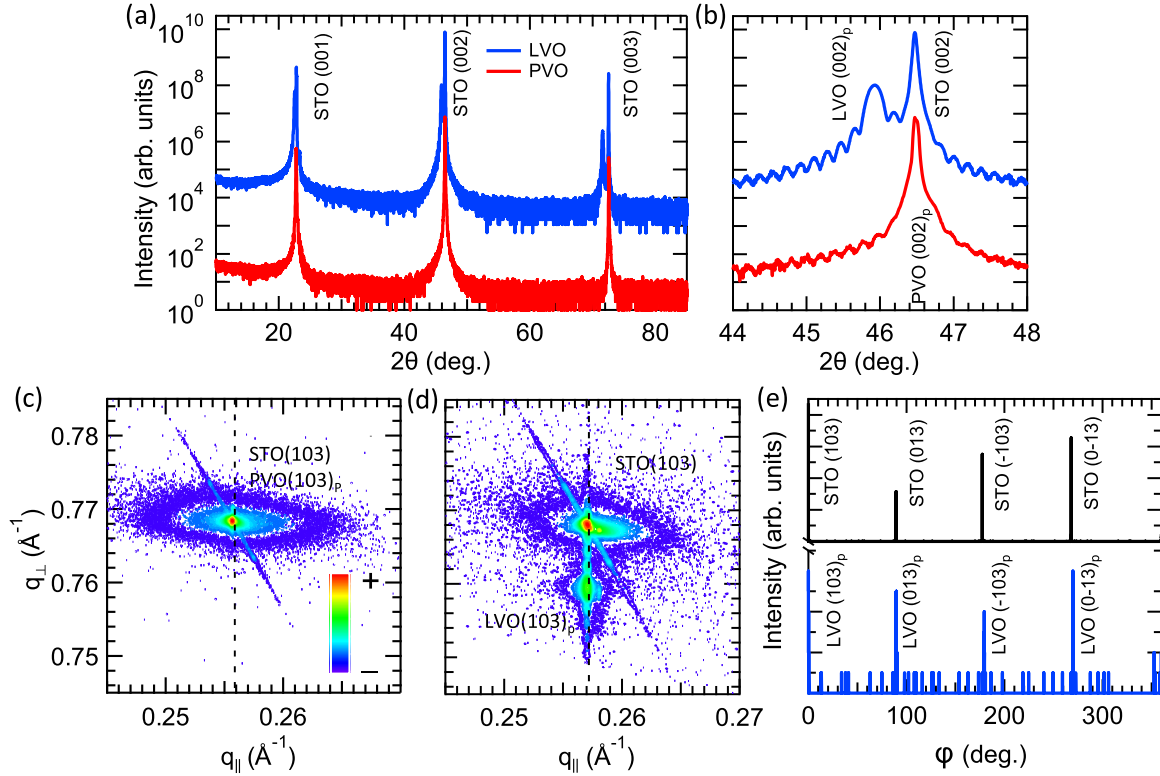


FIG. 2. (a) $\theta - 2\theta$ XRD measurements of thin films in specular geometry around (001), (002), and (003) substrate reflections. (b) $\theta - 2\theta$ measurements in the vicinity of the pseudocubic (002) reflection. Clear Laue fringes are seen and indicate good crystalline and interface quality. (c) and (d) reciprocal space maps around the (103) pseudocubic reflection for PVO and LVO, respectively. PVO and STO superimposed Bragg's peaks and LVO and STO Bragg's peaks aligned along the vertical dashed line indicate that the films are fully strained. (e) φ -scans of the (103)_p LVO and (103) STO reflections.

signal as observed here for PVO compared to LVO, whose magnetization is about 100 times lower. Indeed, Pr^{3+} has two electrons in the 4f orbitals whereas LVO has none. T_{SO} measured for PVO films is in very good agreement with the bulk ordering temperature reported in literature and is slightly higher (~ 10 K) for LVO films. This mimics the strain state experienced by the films with a moderate tensile stress and a

significant compressive stress for PVO and LVO, respectively. As evidenced in the RVO_3 series with hydrostatic pressure experiments [17,18] and PVO films grown by PLD [29], compressive strain strengthens indeed magnetic interactions and consequently enhances the SO ordering temperature for LVO films. As an oxygen stoichiometry deviation would destabilize magnetic orders (see Ref. [32]), this attest further the good stoichiometry of the PVO and LVO films.

We have further investigated the structure of the films by the HRTEM observations performed on the PVO and LVO cross sections taken along the [010] perovskite zone axis in Figs. 4(a) and 4(b), respectively. We observe microstructural domain arrangements (lateral width is around 40 nm), characterized by a contrast arising from oriented domains with sharp boundaries (white dashed-dotted lines) over the whole thickness of the films. The Fourier transforms (FTs) extracted from the selected areas (colored circles) exhibit extra reflections that are not related to a simple cubic perovskite lattice whose characteristic FT is depicted for STO in Fig. 4(b). On the contrary, the FTs obtained for two adjacent domains show that PVO and LVO possess extra reflections (colored and encircled spots) not related to the perovskite subcell (reflection encircled in white). It can be explained if one considers that PVO and LVO present a distorted perovskite structure involving the AFD rotation of the VO_6 octahedra in a $Pbnm$ symmetry. The FTs can be associated with $[001]_o$ [see V_I and middle right FT in Figs. 4(a) and 4(b)] and $[1\bar{1}0]_o$ [see V_{II} bottom right

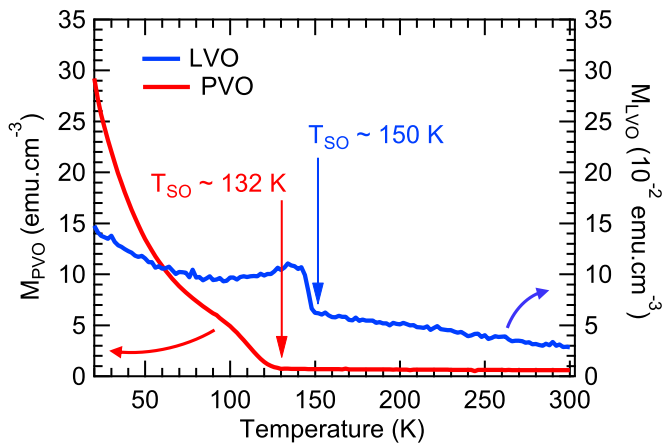


FIG. 3. Magnetization as a function of the temperature from 10 to 300 K after 5000 Oe field cooling from room temperature. The measurements are performed with an applied in-plane magnetic field of 50 Oe. The spin ordering temperatures are indicated by an arrow for each film.

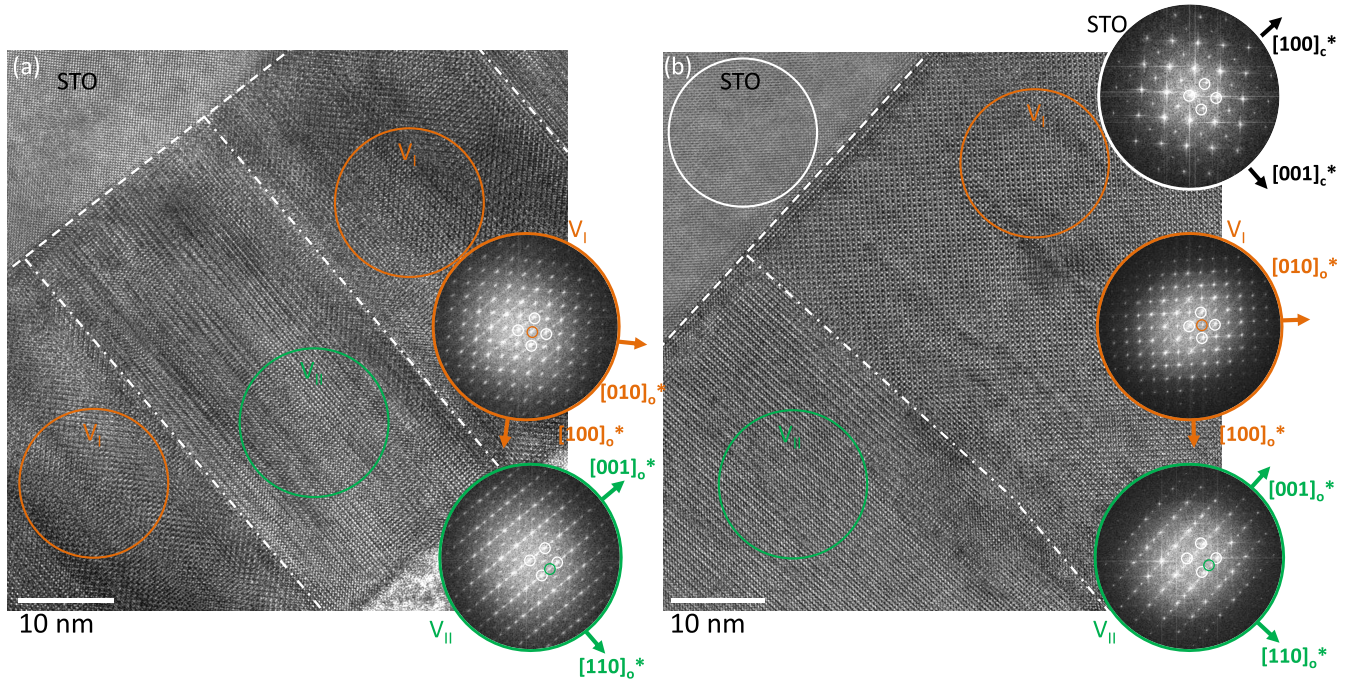


FIG. 4. HRTEM cross-section views along the $[010]$ STO substrate zone axis, for (a) the PVO and (b) the LVO thin film. We notice the films crystallinity and the sharp interfaces with substrate highlighted with dashed white lines. In both thin films two oriented variants, V_I and V_{II} are obtained according to the Fourier transforms (FT) analysis, respectively, in orange circles and green circles. Compared to the FT on the STO substrate in white circle, visible additional reflections are encircled, respectively, in orange and green in V_I and V_{II} FTs. The dashed dotted white lines on the HRTEM pictures border these variants. Such observations are consistent with the epitaxial growth of PVO and LVO orthorhombic cells on the STO cubic structure. The third variant (V_{III}) is in a low proportion in both materials.

FT in Figs. 4(a) and 4(b)] zone axes of a $Pbnm$ structure having cell parameters $a_p\sqrt{2} \times a_p\sqrt{2} \times 2a_p$. The two orientations correspond to the case where $2a_p$ is parallel to the substrate plane but differ by an in-plane rotation of 90° . According to electron microscopy, the epitaxial relationship agrees with $\text{PrVO}_3(\text{LaVO}_3)[110]_o\|\text{SrTiO}_3[001]_c$ and $\text{PrVO}_3(\text{LaVO}_3)[001]_o\|\text{SrTiO}_3[010]_c$ (V_I) or $\text{PrVO}_3(\text{LaVO}_3)[001]_o\|\text{SrTiO}_3[100]_c$ (V_{II}) (also inferred from the RHEED observations). Although V_I and V_{II} are more stable on STO [28,32], a minor proportion of the third variant (V_{III}) having $2a_p$ perpendicular to the plane of the substrate (not shown) has been found corresponding to the epitaxial relationship $\text{PrVO}_3(\text{LaVO}_3)[001]_o\|\text{SrTiO}_3[001]_o$. We note that the growth of strained PVO and LVO on STO would also imply a distortion of the orthorhombic cell through the strain accommodation by the free $[100]_o$, $[010]_o$ axes and the angle between them [26,42] in the case of V_I and V_{II} . Then, the strain imposed by the substrate would lower the $Pbnm$ symmetry to $P2_1/m$ with $\gamma \neq 90^\circ$. We note that the absence of peak splitting in the $(103)_c$ reflection measured in RSM and in φ -scan suggests that the value of a_o and b_o are close to each other (see Supplemental Material of Ref. [32]). The epitaxial relationship we evidence here implies a tilt system $a^-b^+a^-$ as observed and calculated for LVO on STO substrate [26,27,43].

To gain insights on the microstructure and atomic displacements, HAADF-STEM imaging was performed on the PVO and LVO films, whose images are displayed in

Figs. 5(a) and 5(c), respectively. The film/substrate interface is sharp and confirms the epitaxial growth of the films onto STO. In the inset of Figs. 5(a) and 5(c), the PVO and LVO atomic arrangements are represented on a magnified area. For both, we observe vertical Pr and La displacements along lines. These up and down displacements are depicted by superimposed red (Pr) and blue (La) patterns. In order to highlight the cation positions, we have carried out a numerical analysis of the STEM images allowing a quantification of each La and Pr column positions. The atomic positions are extracted and compared with an undistorted reference, which is the STO substrate [44]. The atomic displacement maps across the substrate/film interface are shown in Figs. 5(b) and 5(d) for PVO and LVO, respectively. We see that there is no difference in contrast between the substrate chosen as reference (green) and the first layers. However, we observe an alternating contrast across the film, along the in-plane direction, corresponding to ± 13 – 14 pm La and Pr average motions. This is characteristic of the X_5^- mode with the long orthorhombic c_o axis lying in-plane (in agreement with RHEED and HRTEM observations). Due to the domain arrangement, this characteristic X_5^- mode is observed for PVO and LVO $[001]_o$ direction lying in the cross-section plane and corresponds to V_{II} in Fig. 4. However, the X_5^- mode along the atomic columns direction, corresponding to V_I in Fig. 4, cannot be revealed because the atomic positions are averaged along these directions, attesting to the robustness of our analysis. We point out that no significant V displacements are observed within the

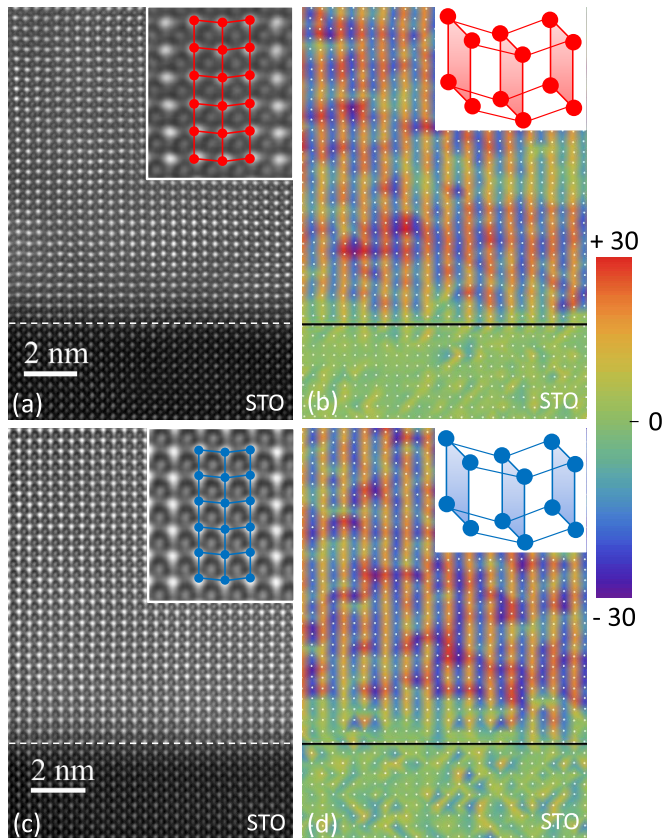


FIG. 5. HAADF-STEM observations for (a) PVO and (c) LVO at the interface with STO, along the [010] STO zone axis. Magnified STEM images showing the La and Pr displacements corresponding to the X_5^- mode. Analysis of the La and Pr displacements for PVO and LVO from the STEM images in (b) and (d), respectively. The color scale indicate the relative displacements in picometer. An illustration of the X_5^- displacement is represented in inset (considering the film/substrate epitaxial relationship).

accuracy of this numerical analysis. Finally, we show that the rare-earths displacements natively exist in RVO_3 thin films.

To summarize, high crystalline PVO and LVO thin films were obtained on (001)-oriented STO substrate by molecular

beam epitaxy. A layer-by-layer growth mode was evidenced by electron diffraction, which allows us to control the thickness at one pseudocubic cell accuracy. An analysis of the RHEED intensity oscillation period allowed us to rationalize the optimized condition for a stoichiometric growth. According to the HRTEM observations, the film microstructure is characterized by different oriented domains, for both PVO and LVO. These domains differ by an in-plane 90° rotation owing the STO surface fourfold symmetry. We have measured the magnetic transition of the films at T_{SO} and we have observed the effect of the strain state on the spin ordering temperature. Finally, we have evidenced the rare-earths atomic displacements, which agree with the X_5^- distortion mode in the perovskite cells. Reproducing such an atomic arrangement in superlattices may lead to asymmetric stacks necessary to create electrical dipolar distribution in a magnetic system. As the SO and OO orders are coupled in RVO_3 and potentially tunable by electric polarization, it is a step towards controllable magnetoelectric RVO_3 based systems. The investigation of the structural distortions and atomic displacements in RVO_3 thin films may also be generalized to other orthorhombic $Pbnm$ perovskite oxides.

ACKNOWLEDGMENTS

The authors thank the collaborators of the IJL competence centers D_{avm}, 3M and X-Gamma, in particular S. Migot, S. Robert, G. Medjahdi, and P. Boulet. We thank also N. Viart for helpful discussions. G.M. acknowledges M. Massouras and D. Lacour for their help with AFM measurements and the development of the code for STEM images analysis. This work is supported by the ANR-Labcom Project LSTNM, by the impact project of the French PIA project Lorraine Université d'Excellence, reference ANR-15-IDEX-04-LUE. Experiments were performed using equipment from the TUBE-D_{avm} funded by the FEDER-FSE Lorraine and Massif Vosges 2014-2020 (a European Union Program), the Région Grand Est, and the Métropole Grand Nancy.

- [1] M. Imada, A. Fujimori, and Y. Tokura, *Rev. Mod. Phys.* **70**, 1039 (1998).
- [2] Y. Tokura and N. Nagaosa, *Science* **288**, 462 (2000).
- [3] P. Zubko, S. Garaglio, M. Gabay, P. Ghosez, and J.-M. Triscone, *Annu. Rev. Condens. Matter Phys.* **2**, 141 (2011).
- [4] M. H. Sage, G. R. Blake, C. Marquina, and T. T. M. Palstra, *Phys. Rev. B* **76**, 195102 (2007).
- [5] J.-S. Zhou, J. A. Alonso, V. Pomjakushin, J. B. Goodenough, Y. Ren, J.-Q. Yan, and J.-G. Cheng, *Phys. Rev. B* **81**, 214115 (2010).
- [6] J.-S. Zhou and J. B. Goodenough, *Phys. Rev. Lett.* **94**, 065501 (2005).
- [7] J.-S. Zhou and J. B. Goodenough, *Phys. Rev. B* **77**, 132104 (2008).
- [8] S. Miyasaka, Y. Okimoto, M. Iwama, and Y. Tokura, *Phys. Rev. B* **68**, 100406(R) (2003).
- [9] J.-S. Zhou and J. B. Goodenough, *Phys. Rev. Lett.* **96**, 247202 (2006).
- [10] J. B. Goodenough, *Rev. Prog. Phys.* **67**, 1915 (2004).
- [11] E. Dagotto, *Science* **309**, 257 (2005).
- [12] E. Bousquet, M. Dawber, N. Stucki, C. Lichtensteiger, P. Hermet, S. Gariglio, J.-M. Triscone, and Ph. Ghosez, *Nature (London)* **452**, 732 (2008).
- [13] N. A. Benedek and C. J. Fennie, *Phys. Rev. Lett.* **106**, 107204 (2011).
- [14] J. M. Rondinelli and C. J. Fennie, *Adv. Mater.* **24**, 1961 (2012).
- [15] J. Varignon, N. C. Bristowe, E. Bousquet, and Ph. Ghosez, *Sci. Rep.* **5**, 15364 (2015).

- [16] J. Fujioka, S. Miyasaka, and Y. Tokura, *Phys. Rev. B* **72**, 024460 (2005).
- [17] J.-S. Zhou, J. B. Goodenough, J.-Q. Yan, J.-G. Cheng, K. Matsubayashi, Y. Uwatoko, and Y. Ren, *Phys. Rev. B* **80**, 224422 (2009).
- [18] D. Bizen, K. Nakatsuka, T. Murata, H. Nakao, Y. Murakami, S. Miyasaka, and Y. Tokura, *Phys. Rev. B* **78**, 224104 (2008).
- [19] Y. Ren, T. T. M. Palstra, D. I. Khomskii, E. Pellegrin, A. A. Nugroho, A. A. Menovsky, and G. A. Sawatzky, *Nature (London)* **396**, 441 (1998).
- [20] L. Wang, Y. Li, A. Bera, C. Ma, F. Jin, K. Yuan, W. Yin, A. David, W. Chen, W. Wu, W. Prellier, S. Wei, and T. Wu, *Phys. Rev. Appl.* **3**, 064015 (2015).
- [21] H.-T. Zhang, M. Brahlek, X. Ji, S. Lei, J. Lapano, J. W. Freeland, V. Gopalan, and R. Engel-Herbert, *ACS Appl. Mater. Interfaces* **9**, 12556 (2017).
- [22] Y. Hotta, T. Susaki, and H. Y. Hwang, *Phys. Rev. Lett.* **99**, 236805 (2007).
- [23] J.-S. Zhou, J. B. Goodenough, J.-Q. Yan, and Y. Ren, *Phys. Rev. Lett.* **99**, 156401 (2007).
- [24] Y. Hotta, Y. Mukunoki, T. Susaki, and H. Y. Hwang, *Appl. Phys. Lett.* **89**, 031918 (2006).
- [25] H.-T. Zhang, L. R. Dedon, L. W. Martin, and R. Engel-Herbert, *Appl. Phys. Lett.* **106**, 233102 (2015).
- [26] H. Rotella, U. Lüders, P.-E. Janolin, V. H. Dao, D. Chateigner, R. Feyerherm, E. Dudzik, and W. Prellier, *Phys. Rev. B* **85**, 184101 (2012).
- [27] H. Rotella, O. Copie, G. Steciuk, H. Ouerdane, P. Boullay, P. Roussel, M. Morales, A. David, A. Pautrat, B. Mercey, L. Lutterotti, D. Chateigner, and W. Prellier, *J. Phys.: Condens. Matter* **27**, 175001 (2015).
- [28] H. Meley, Karandeep, L. Oberson, J. de Bruijckere, D. T. L. Alexander, J.-M. Triscone, Ph. Ghosez, and S. Gariglio, *APL Mater.* **6**, 046102 (2018).
- [29] D. Kumar, A. David, A. Fouchet, A. Pautrat, J. Varignon, C. U. Jung, U. Lüders, B. Domengès, O. Copie, P. Ghosez, and W. Prellier, *Phys. Rev. B* **99**, 224405 (2019).
- [30] D. Kumar, A. Fouchet, A. David, A. Cheikh, T. S. Suraj, O. Copie, C. U. Jung, A. Pautrat, M. S. Ramachandra Rao, and W. Prellier, *Phys. Rev. Mater.* **3**, 124413 (2019).
- [31] O. Copie, H. Rotella, P. Boullay, M. Morales, A. Pautrat, P.-E. Janolin, I. C. Infante, D. Pravathana, U. Lüders, and W. Prellier, *J. Phys.: Condens. Matter* **25**, 492201 (2013).
- [32] O. Copie, J. Varignon, H. Rotella, G. Steciuk, Ph. Boullay, A. Pautrat, A. David, B. Mercey, Ph. Ghosez, and W. Prellier, *Adv. Mater.* **29**, 1604112 (2017).
- [33] See Supplemental Material at <http://link.aps.org/supplemental/10.1103/PhysRevMaterials.4.064417> for further details on the AFM images of the LVO and PVO surfaces.
- [34] M. Brahlek, L. Zhang, H.-T. Zhang, J. Lapano, L. R. Dedon, L. W. Martin, and R. Engel-Herbert, *Appl. Phys. Lett.* **109**, 101903 (2016).
- [35] L. D. Tung, *Phys. Rev. B* **72**, 054414 (2005).
- [36] A. V. Mahajan, D. C. Johnston, D. R. Torgeson, and F. Borsa, *Phys. Rev. B* **46**, 10966 (1992).
- [37] M. Onodo and H. Nagasawa, *Solid State Commun.* **99**, 487 (1996).
- [38] Y. Kimishima, Y. Ichianagi, K. Shimizu, and T. Mizuno, *J. Magn. Magn. Mater.* **210**, 244 (2000).
- [39] M. Reehuis, C. Ulrich, P. Pattison, B. Ouladdiaf, M. C. Rheinstädter, M. Ohl, L. P. Regnault, M. Miyasaka, Y. Tokura, and B. Keimer, *Phys. Rev. B* **73**, 094440 (2006).
- [40] M. Reehuis, C. Ulrich, K. Prokeš, S. Mat'aš, J. Fujioka, S. Miyasaka, Y. Tokura, and B. Keimer, *Phys. Rev. B* **83**, 064404 (2011).
- [41] M. Reehuis, C. Ulrich, P. M. Abdala, P. Pattison, G. Khaliullin, J. Fujioka, S. Miyasaka, Y. Tokura, and B. Keimer, *Phys. Rev. B* **94**, 104436 (2016).
- [42] A. Vailionis, H. Boschker, W. Siemons, E. P. Houwman, D. H. A. Blank, G. Rijnders, and G. Koster, *Phys. Rev. B* **83**, 064101 (2011).
- [43] G. Schlauzero and C. Ederer, *Phys. Rev. B* **92**, 235112 (2015).
- [44] The pixel intensity analysis of the HAADF images determines the atomic positions and allows us to define a grid of these elements location. For each nodes of the grid, the distances to the first four neighbors are calculated. These distances are converted to picometer (pm) using an STO grid as a reference. The angles between each atomic column and their in plane and out-of-plane two first neighbors were thus extracted. The in-plane and out-of-plane local average positions of the neighboring atoms are thus calculated and yield out-of-plane and in-plane displacements, respectively.